A granular Rayleigh-Taylor instability: experiments and simulations

Jan Ludvig Vinningland,[1, *] Øistein Johnsen,[1] Eirik G. Flekkøy,[1] Renaud Toussaint,[2] and Knut Jørgen Måløy[1]

[1]*Department of Physics, University of Oslo, P.O. Box 1048, N-0316 Oslo, Norway*
[2]*Institut de Physique du Globe de Strasbourg, CNRS, Université Louis Pasteur, 5 rue Descartes, 67084 Strasbourg Cedex, France*
(Dated: October 13, 2006)

A granular instability is studied experimentally and numerically as a packing of dense granular material positioned above a gap of air falls under gravity in a closed Hele-Shaw cell; a granular analog of the Rayleigh-Taylor instability. A characteristic pattern of fingers separated by dilute bubbles emerges along the interface, and, in contrast to the classical, hydrodynamic instability, a transient coarsening of the front is observed. The emerging structures are quantified by means of Fourier analysis and quantitative agreement between experiment and computation is shown. This analysis also reveals scale invariance of the flow structures under overall change of spatial scale.

Granular materials, such as grains or powders, are ubiquitous in nature and are involved in a host of industrial processes [1–3]. Improved understanding of granular flows would be of essential importance to a range of industrial applications, to the study of geological pattern forming processes, and, in general, to the theoretical description of disordered media.

As grains become smaller the effect of the interstitial fluid becomes more important. The result is a combination of dry granular dynamics and the hydrodynamics of the fluid. These systems give rise to a variety of exotic, and most often poorly understood, phenomena such as fluidization [2] and bubble instabilities [4, 5], quicksand and jet formation [6], and sandwich structures in systems where different particle types segregate [7]. While the study of dry granular media has been extensive over the past decades, the exploration of fluid-granular systems has been of more limited scope.

In the present Letter we study a granular analog of the Rayleigh-Taylor instability [8]. The experimental setup consists of a closed Hele-Shaw cell that confines air and fine grains. When the cell is turned upside down we observe the evolution of an initially sharp front formed by the falling grains. This evolution has three stages: (1) An initial decompaction phase is followed by (2) the formation of vertical fingers that organize into cusp-shaped structures, that subsequently develop into (3) coarser finger-bubble structures. The last structures, seen in Fig. 1, represent a quasi steady state where two competing mechanisms produce a characteristic wavelength. The mechanism producing coarser scales originates as smaller bubbles, and the fingers defining them, increasingly lag behind their bigger neighbors, leaving behind a single wide finger in the process, and thereby reducing the total number of fingers. This process resembles the coarsening seen in crystal growth [9]. The other mechanism, that produces finer scales, and is active right from the start, is reminiscent of the tip splitting process seen in viscous fingering. It is manifested as thin filaments forming in the centre of the rising bubbles.

Over the past few years a wide range of granular instabilities where various structures form along fluid-grain interfaces have been reported [4, 5, 10–13]. Notably, the patterns formed by grains falling in a highly viscous liquid were investigated experimentally and theoretically by Völtz et al. [14]. However, while the instability reported by Völtz shares its main qualitative characteristics with the classical Rayleigh-Taylor instability, i.e. a single dominating wavelength growing right from the start in a sinusoidal fashion, our gas-grain instability grows through coarsening cusp-structures.

The coarsening in the present structures suggests that the process is intrinsically non-linear in the sense that linear stability analysis is not an appropriate tool to predict the (time dependent) characteristic scale. However, the evolving structures exhibit scale invariance under change of particle size, a feature which is supported both by observations and theoretical considerations. The simulations and experiments that are employed to shed light on the phenomenon at hand agree qualitatively, and to a significant extent, quantitatively, even though the model neglects both granular friction and the third dimension in the direction normal to the Hele-Shaw cell.

In the experiments the Hele-Shaw cell is made of two glass
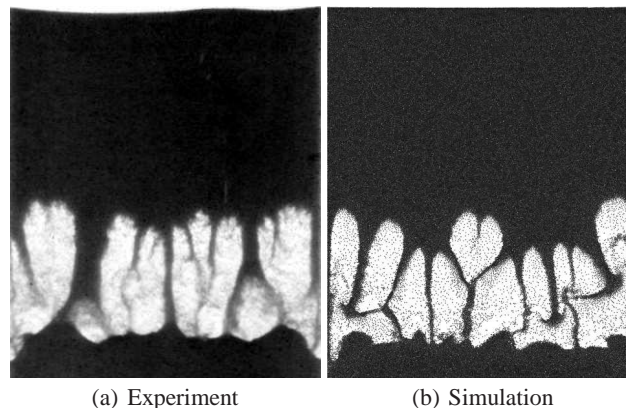

(a) Experiment   (b) Simulation

Figure 1: (a) Experimental image of a vertical Hele-Shaw cell filled with air (white) and polystyrene beads (black) of 140 μm in diameter. The cell is 56 mm wide, and was rotated 0.2 seconds ago. (b) Simultaneous numerical snapshot of the same system.

plates sealed with a silicone gasket along the edges and held together by clamps. The internal dimension of the cell is 56 x 86 x 1 mm. The cell is filled with air at atmospheric pressure and monodisperse polystyrene beads, Dynoseeds TS 140-51, with a mass density of 1.05 g/cm^3. The cell may rotate 130 degrees around a hinged bar from a lower to an upper vertical position where it is stopped by a bar. The rotation is performed manually in about 0.2 seconds. The centrifugal forces slow down the falling motion of the grains during the rotation, even though the falling is not quite suppressed. Images are recorded at a rate of 500 frames per second by a high speed digital camera, Photron Fastcam-APX 120K, with a resolution of 512x512 pixels. Fig. 1a shows an experimental snapshot recorded 0.2 seconds after the cell reached the upright vertical position. For the purpose of comparison with the simultaneous simulation shown in Fig. 1b the colors of the image are inverted.

Numerical investigations of even moderately sized granular systems consumes prohibitive computational resources if the fluid dynamics is described on a sub-granular level. The numerical model employed here combines a continuum description of the air with a discrete description of the granular phase. The derivation and theoretical justification of the model are presented in detail in Ref. [15, 16]. The effect of the granular phase on the air pressure is that of a deformable porous medium locally defined by the granular packing. The granular phase is modeled as discrete particles from which a coarse grained solid fraction $\rho(x, y)$ and a velocity field $\mathbf{u}(x, y)$ are obtained. The continuum gas phase is described solely by its pressure $P(x, y)$. The inertia, and hence the velocity field of the gas, is neglected. This is justified as long as the particle Reynolds number is small, which is fulfilled in our case. The pressure is governed by the equation [15, 16]

$$\phi\left(\frac{\partial P}{\partial t} + \mathbf{u} \cdot \boldsymbol{\nabla} P\right) = \boldsymbol{\nabla} \cdot \left(P\frac{\kappa}{\mu}\boldsymbol{\nabla} P\right) - P\boldsymbol{\nabla} \cdot \mathbf{u}, \quad (1)$$

where $\phi = 1 - \rho$ is the porosity, κ the permeability, $\mathbf{u}$ the velocity field of the granular phase, and μ the gas viscosity. This equation is derived from the continuity of air and grain mass, and Darcy's law [17] with permeability κ. The Carman-Kozeny relation [18] is assumed for the permeability, and the isothermal ideal gas law for the air. The grains are governed by Newtons second law

$$m\frac{d\mathbf{v}}{dt} = m\mathbf{g} + \mathbf{F}_{\mathrm{I}} - \frac{\boldsymbol{\nabla} P}{\rho_n}, \quad (2)$$

where m is the grain mass, $\mathbf{v}$ is the grain velocity, $\mathbf{F}_{\mathrm{I}}$ is the interparticle force which keeps the grains from overlapping, $\rho_n = \rho\,\rho_g/m$ is the number density, and ρ_g is the mass density of the material which the grains are made of. Contact dynamics [19] is used to calculate the interparticle force $\mathbf{F}_{\mathrm{I}}$. The dynamics of the grains are simplified by neglecting particle-particle and particle-wall friction. A lower cutoff is imposed on the solid fraction because the Carman-Kozeny relation is not valid as the solid fraction drops below 0.25. This cutoff causes the permeability of the most dilute regions of the

system to be slightly lower than the true permeability, which again causes the pressure gradients, and hence the force acting on the grains in these regions, to be slightly overestimated. This is further discussed in connection with Fig. 5a.

The numerical snapshot in Fig. 1b shows a typical pattern obtained in a simulation using grains of the same diameter and density as in the experiment in Fig. 1a. The main features of the experimentally observed structures, i.e. the number of bubbles, the tip splitting and finger nucleation processes, are well reproduced in the simulations.

The spatio-temporal evolution of the interface in the experiment and simulation is presented in Figs. 2a and 2b, respectively. The interface moves upwards in these plots with a temporal separation of 0.024 seconds, and the first and last interfaces are extracted at 0.002 and 0.290 seconds, respectively. The interface is determined by the following procedure. A thresholding of the numerical solid fraction field is performed by vertical scans initiated from the top, and the interface is defined as the nodes where the solid fraction drops below a certain value. For the experimental data the thresholding is performed on the pixel values of the images. There is an inverse relationship between the pixel values and the solid fraction, i.e. dilute regions with low solid fraction appear as white in the images with high pixel values, and vice versa.

The shape of the initial interfaces in Figs. 2a and 2b are quite different. The initial experimental interface has noise on all wavelengths, whereas the initial numerical interface is virtually flat with noise dominantly at smaller wavelengths. Perturbations introduced in the cell by the rotation and sudden stop disturb the initial experimental interface. However, as the instability evolves the discrepancy reduces, and the later interfaces are more consistent.

In order to give a more quantitative comparison of the interfaces, the discrete Fourier transform [20] is applied on every second interface in Fig. 2 to produce the power spectra presented in Fig. 3. The power spectra are colored as their corresponding interfaces, and the location of the maximum wave number for each power spectrum is indicated by a circle. While the maximum wave number of the numerical interfaces moves from high values to low values, the maximum wave number of the experimental interfaces hardly moves at all, most likely because the experiment does not evolve from an initially flat interface. However, the experimental and numerical power spectra converge to approximately the same form when normalized.

In order to see the coarsening of the experimental structure quantitatively we perform an average over the entire system. The discrete Fourier transform [20] and the power spectrum of each horizontal line of the solid fraction is calculated. Then the averaged power spectrum, $\bar{S}(k)$, is obtained by averaging over these horizontal power spectra, and an average wave number is defined as $\langle k \rangle = \sum_k \bar{S}(k) \cdot k / \sum_k \bar{S}(k)$. Likewise, we define the squared standard deviation $\sigma_k{}^2 = \sum_k \bar{S}(k) \cdot k^2 / \sum_k \bar{S}(k) - \langle k \rangle^2$. For the experimental data the image pixel values are used to estimate the solid fraction.
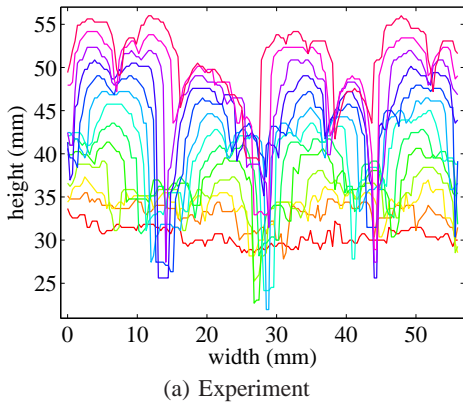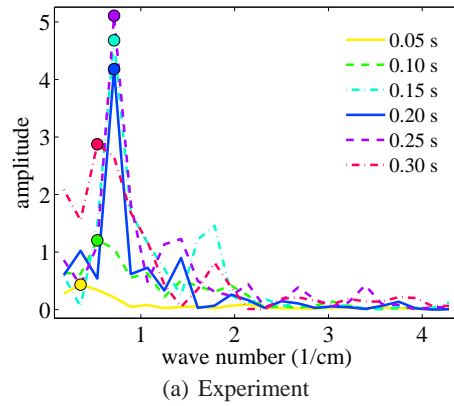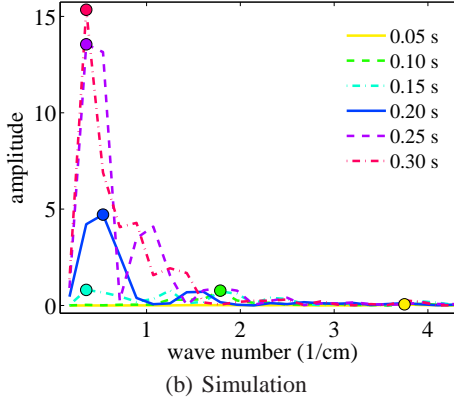
(a) Experiment
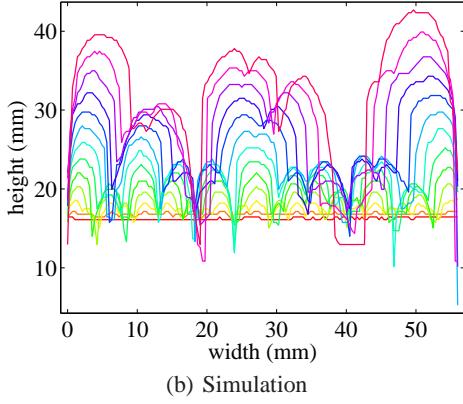
(b) Simulation

Figure 2: The spatio-temporal evolution of (a) the experimental interface and (b) the numerical interface. The interface moves upwards, and the temporal separation of the plots is 0.024 seconds. Notice the emergence of new fingers on the later interfaces.

(a) Experiment

(b) Simulation

Figure 3: The temporal evolution of the interfacial power spectrum for (a) the experiment and (b) the simulation. The times are given in the legend box, and the circles indicate the location of the maximum wave number for each power spectrum.
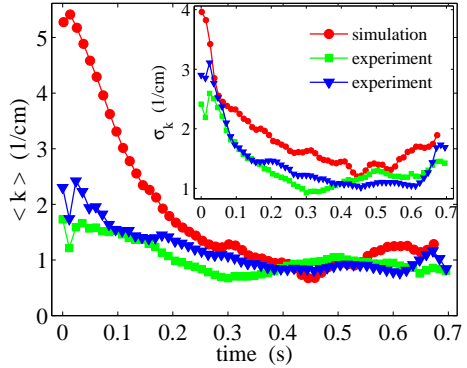
Fig. 4 shows the temporal evolution of $\langle k \rangle$ and σ_k (inset) for the numerical and experimental data. An additional set of experimental data are added to the plot. The numerical curve starts out with a significantly higher wave number than the experimental curves, and it decreases monotonously until it coincides with the experimental curve at about 0.2 seconds, after which the simulation and experiments show a similar coarsening behavior. No fingers are observed in the experiment until 0.06 seconds have elapsed. During this time the grains merely form a dilute sheet of grains that appears homogeneous on the experimental images. This particular experimental initial state is caused by the sudden stop of the cell, and is the most probable reason for the initial discrepancy between simulation and experiment in Fig. 4. The fluctuations of $\langle k \rangle$ and σ_k are associated with the continuous nucleation and merging of fingers.

We investigate the behavior of the system as the overall scale is changed. Since all length ratios and the particle number are fixed, the size of the system scales according to the diameter d of the grains. We measure the characteristic inverse length scale $\langle k \rangle$ as d is changed and observe a scale invariance of the evolution. A series of seven simulations are performed where d varies from 70 μm to 490 μm in steps of 70 μm. The size of the cell containing grains of 70 μm in diam-

Figure 4: Mean wave number $\langle k \rangle$ and standard deviation σ_k (inset) for two experiments and one simulation, all using polystyrene beads of 140 μm in diameter.

eter is 28 x 34 mm. In these simulations we have introduced the larger density of glass, rather than polystyrene, in order to minimize the numerical artifacts associated with the solid fraction cutoff in the permeability. To compare, a series of experiments using polystyrene beads of 80, 140, 230, and 500 μm in diameter, confined in Hele-Shaw cells that scale with d in all directions, are performed. Data-collapse plots of the
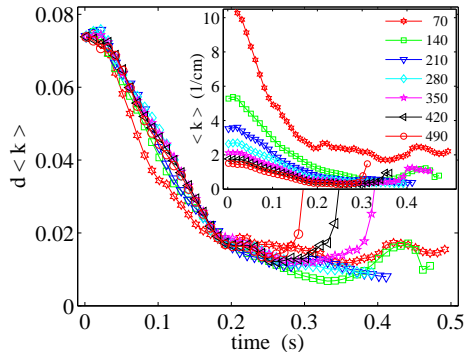
(a) Simulation
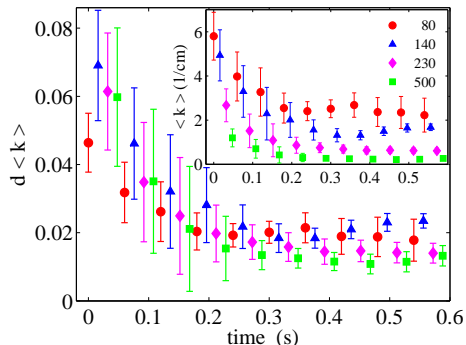
(b) Experiment

Figure 5: Data-collapse of $d\langle k\rangle$ for a series of (a) simulations using glass beads, and (b) experiments using polystyrene beads. The grain diameters d are given in units of µm in the legend box. The inset shows the evolution of $\langle k\rangle$.

rescaled mean wave number $d\langle k\rangle$ are shown in Figs. 5a and 5b for the simulations and experiments, respectively. These plots indicate that the characteristic size of the structures is invariant when the size is measured in units of d; the number of grains that spans the width of the bubbles is the same for a wide range of grain sizes.

Theoretically, the scale invariance of the product $d\langle k\rangle$ may be interpreted as follows: Compared to the other terms of Eqs. (1) and (2) the $m\,d\mathbf{v}/dt$, F_{I} and $P\nabla\cdot\mathbf{u}$ terms may be shown to be small [21]. For that reason, these equations exhibit an approximate invariance under system size scaling. If we take δP to be the pressure deviation from the background pressure, express the velocity of grain i as $\mathbf{v}_i = \delta\mathbf{v}_i + \mathbf{u}_0$ and the locally averaged granular velocity as $\mathbf{u} = \delta\mathbf{u} + \mathbf{u}_0$, where $\mathbf{u}_0$ is the constant sedimentation velocity of a close packed system, this scaling may be expressed as $\mathbf{x} \rightarrow \lambda\mathbf{x}$, $\delta P \rightarrow \lambda\delta P$, $\mathbf{u}_0 \rightarrow \lambda^2\mathbf{u}_0$, $\delta\mathbf{u} \rightarrow \lambda\delta\mathbf{u}$ and $\kappa \rightarrow \lambda^2\kappa$, where λ is a scale factor. The structure formation of the system is governed by $\delta\mathbf{u}$ and, since this velocity scales the same way with λ as the length scales themselves, the evolution of any structure measured in units of d will be scale invariant. In particular this is true for the structures measured by the length $1/\langle k\rangle$, and so $d\langle k\rangle$ is scale invariant. However, the invariance deteriorates both when particle size is increased, and when it is decreased. In the first case, the relative effect of granular inertia is increased, in the second, the relative effect of the $P\nabla\cdot\mathbf{u}$ term is increased.

The convergence of the numerical data-collapse is quite good, whereas the experimental data-collapse has a wider distribution but collapses satisfactorily given the standard deviation error bars. The deviation of the 70 µm curve of Fig. 5 is probably explained by the increase in the relative importance of the $P\nabla\cdot\mathbf{u}$-term. The divergences of the 350, 420, and 490 µm curves in the same plot arise because the bubbles in the coarser packings disappear before they reach the surface due to the increase of $\mathbf{u}_0$ with λ^2 [21]. The experimental data presented in Fig. 5b is obtained by averaging over three experiments. The standard deviation is calculated over a time window of 0.3 seconds and is represented by the error bars. The accuracy of the experiments is at its lowest during the initial coarsening of the structures. As the mean wave number stabilizes around 0.2 seconds the accuracy improves, except for the 80 µm curve. Nevertheless, the data points are, with a few exceptions, within a distance of one standard deviation from one another. The loss of precision for small times is most likely caused by the inaccuracy involved with the manual rotation.

In conclusion we have presented experimental and numerical results of a granular flow instability which is significantly different from its classical hydrodynamic analog. The simulations reproduce the characteristic shape and size of the experimentally observed structures, and provide patterns in the early phase of the process, which is not resolved experimentally. Data-collapse plots of the mean wave number indicates that the flow and resulting structures are invariant when measured on a scale proportional to the grain diameter for a range of diameters that spans from 70 µm to 500 µm.

* Electronic address: janlv@fys.uio.no

[1] H. J. Herrmann, J.-P. Hovi, and S. Luding, eds., *Physics of Dry Granular Media*, vol. 350 of *NATO ASI Series E: Applied Sciences* (Kluwer Academic Publishers, Dordrecht, 1998).

[2] J. F. Davidson and D. Harrison, *Fluidization* (Academic Press, New York, 1971).

[3] D. Gidaspow, *Multiphase Flow and Fluidization* (Academioc Press, San Diego, 1994).

[4] D. Gendron, H. Troadec, K. J. Måløy, and E. G. Flekkøy, Phys. Rev. E **64**, 021509 (2001).

[5] E. G. Flekkøy, S. McNamara, K. J. Måløy, and D. Gendron, Phys. Rev. Lett. **87**, 134302 (2001).

[6] D. Lohse, R. Rauhé, R. Bergmann, and D. van der Meer, Nature **432**, 689 (2004).

[7] C. Zeilstra, M. A. van der Hoef, and J. A. M. Kuipers, Phys. Rev. E **74**, 010302 (2006).

[8] G. Taylor, Proc. Roy. Soc. A **201**, 192 (1950).

[9] J. S. Langer, Rev. Mod. Phys. **52**, 1 (1980).

[10] C. Chevalier, M. B. Amar, D. Bonn, and A. Lindner, J. Fluid Mech. **552**, 83 (2006).

[11] Ø. Johnsen, R. Toussaint, K. J. Måløy, and E. G. Flekkøy, Phys. Rev. E **74**, 011301 (2006).

[12] M. P. Ciamarra, A. Coniglio, and M. Nicodemi, J. Phys.: Con-

dens. Matter **17**, 2549 (2005).

[13] F. Malloggi, J. Lanuza, B. Andreotti, and E. Clement, Europhys. Lett. **75**, 825 (2006).

[14] C. Völtz, W. Pesch, and I. Rehberg, Phys. Rev. E **65**, 011404 (2001).

[15] S. McNamara, E. G. Flekkøy, and K. J. Måløy, Phys. Rev. E **61**, 4054 (2000).

[16] D.-V. Anghel, M. Strauss, S. McNamara, E. G. Flekkøy, and K. J. Måløy, Phys. Rev. E **74**, 029906(E) (2006).

[17] H. Darcy, *Les Fontaines Publiques de la Ville de Dijon* (Dalmont and Paris, 1856).

[18] P. C. Carman, Trans. Inst. Chem. Eng. **15**, 150 (1937).

[19] F. Radjai, M. Jean, J.-J. Moreau, and S. Roux, Phys. Rev. Lett. **77**, 274 (1996).

[20] W. H. Press, S. A. Teukolsky, W. T. Vetterling, and B. P. Flannery, *Numerical Recipes in C++* (Cambridge University Press, 2002), chap. 12. Fast Fourier Transform, p. 505.

[21] J. L. Vinningland, Ø. Johnsen, E. G. Flekkøy, R. Toussaint, and K. J. Måløy, Phys. Rev. E (to be published).